MAGNETIC RESONANCE IN CHEMISTRY
Magn. Reson. Chem. 2005; **43**: S4–S19
Published online in Wiley InterScience (www.interscience.wiley.com). DOI: 10.1002/mrc.1690

Combining high-field EPR with site-directed spin labeling reveals unique information on proteins in action†

K. Möbius,[1]* A. Savitsky,[1] C. Wegener,[2] M. Plato,[1] M. Fuchs,[1] A. Schnegg,[1] A. A. Dubinskii,[3] Y. A. Grishin,[4] I. A. Grigor'ev,[5] M. Kühn,[2] D. Duché,[6] H. Zimmermann[7] and H.-J. Steinhoff[2]

[1] Fachbereich Physik, Freie Universität Berlin, Arnimallee 14, D-14195 Berlin, Germany
[2] Fachbereich Physik, Universität Osnabrück, Barbarastr. 7, D-49069 Osnabrück, Germany
[3] Semenov Institute of Chemical Physics, Kosygina str. 4, 117977 Moscow, Russia
[4] Institute of Chemical Kinetics and Combustion, Institutskaya str. 3, 630090 Novosibirsk, Russia
[5] Institute of Organic Chemistry, Akad. Lavrent'ev Ave. 9, 630090 Novosibirsk, Russia
[6] Laboratoire d'Ingénierie des Systèmes Macromoléculaires, Institut de Biologie Structurale et Microbiologie, CNRS, 31 chemin Joseph Aiguier, F-13402, Marseille cedex 20, France
[7] Abteilung Biomedizinische Optik, Max-Planck-Institut für Medizinische Forschung, Jahnstr. 29, D-69120 Heidelberg, Germany

Received 9 May 2005; Accepted 10 June 2005

In the last decade, joint efforts of biologists, chemists and physicists have helped in understanding the dominant factors determining specificity and directionality of transmembrane transfer processes in proteins. In this endeavor, electron paramagnetic resonance (EPR) spectroscopy has played an important role. Characteristic examples of such determining factors are hydrogen-bonding patterns and polarity effects of the microenvironment of protein sites involved in the transfer process. These factors may undergo characteristic changes during the reaction and, thereby, control the efficiency of biological processes, e.g. light-induced electron and proton transfer across photosynthetic membranes or ion-channel formation of bacterial toxins. In case the transfer process does not involve stable or transient paramagnetic species or states, site-directed spin labeling with suitable nitroxide radicals still allows EPR techniques to be used for studying structure and conformational dynamics of the proteins in action. By combining site-directed spin labeling with high-field/high-frequency EPR, unique information on the proteins is revealed, which is complementary to that of X-ray crystallography, solid-state NMR, FRET, fast infrared and optical spectroscopic techniques. The main object of this publication is twofold: (i) to review our recent spin-label high-field EPR work on the bacteriorhodopsin light-driven proton pump from *Halobacterium salinarium* and the Colicin A ion-channel forming bacterial toxin produced in *Escherichia coli*, (ii) to report on novel high-field EPR experiments for probing site-specific pK_a values in protein systems by means of pH-sensitive nitroxide spin labels. Taking advantage of the improved spectral and temporal resolution of high-field EPR at 95 GHz/3.4 T and 360 GHz/12.9 T, as compared to conventional X-band EPR (9.5 GHz/0.34 T), detailed information on the transient intermediates of the proteins in biological action is obtained. These intermediates can be observed and characterized while staying in their working states on biologically relevant timescales. The paper concludes with an outlook of ongoing high-field EPR experiments on site-specific protein mutants in our laboratories at FU Berlin and Osnabrück.

KEYWORDS: high-field EPR; site-directed spin labeling; transmembrane proteins; proton transport; ion-channel formation

INTRODUCTION

In proteomics research, present day interdisciplinary collaboration of chemists, physicists and biologists aims at a better understanding of the structure–dynamics–function relationship of proteins that controls important biological processes on the molecular level. In this demanding endeavor, in addition to molecular biology, specific techniques in molecular spectroscopy turned out to be well suited to provide essential information complementary to that obtained by X-ray, neutron and electron diffraction methodologies. Examples are fast optical spectroscopy in the visible and IR regions,[1–4] FRET,[5] liquid- and solid-state NMR,[6–8] and multi-frequency electron paramagnetic

†**Presented as part of a special issue on High-field EPR in Biology, Chemistry and Physics.**

*Correspondence to: K. Möbius, Fachbereich Physik, Freie Universität Berlin, Arnimallee 14, D-14195 Berlin, Germany.
E-mail: moebius@physik.fu-berlin.de

Contract/grant sponsor: Deutsche Forschungsgemeinschaft–the Schwerpunktprogramm; Contract/grant number: SPP 1051.

resonance (EPR).[9–12] In conjunction with molecular engineering to generate site-specific mutants with tailor-made spin labels or isotopes, controlled modifications of the protein and their effects on the biological process can be studied to great detail.

The information content of EPR spectra is governed by the static spin Hamiltonian, $\hat{H}_0$, consisting of three terms (for $S = 1/2$ systems):

$$\hat{H}_0/h = \frac{\mu_B}{h} \cdot \mathbf{B}_0 \cdot \tilde{\mathbf{g}} \cdot \hat{\mathbf{S}} - \sum_i \frac{g_{ni} \cdot \mu_K}{h} \cdot \mathbf{B}_0 \cdot \hat{\mathbf{I}}_i + \sum_i \hat{\mathbf{S}} \cdot \tilde{\mathbf{A}}_i \cdot \hat{\mathbf{I}}_i \quad (1)$$

i.e. the field-dependent electron and nuclear Zeeman interactions and the field-independent electron-nuclear hyperfine interactions (h: Planck constant; μ_B, μ_K: Bohr and nuclear magnetons; g_n: nuclear g-factors; $\hat{\mathbf{S}}$, $\hat{\mathbf{I}}$: electron and nuclear spin vector operators; the summation is over all nuclei).

The interaction tensors $\tilde{\mathbf{g}}$ and $\tilde{\mathbf{A}}_i$ probe the electronic structure (wave function) of the molecule either *globally* ($\tilde{\mathbf{g}}$ tensor) or *locally* (hyperfine tensors). The tensors contain isotropic and anisotropic contributions. In isotropic fluid solution, only the scalar values, $1/3 \cdot \mathrm{Tr}(\tilde{\mathbf{g}})$ and $1/3 \cdot \mathrm{Tr}(\tilde{\mathbf{A}})$, are observed. In frozen solutions, powders or single crystals, on the other hand, anisotropic tensor contributions also become observable provided appropriate resolution conditions prevail.

For low-symmetry systems, particularly in frozen solution samples, standard EPR suffers from low spectral resolution because of strong inhomogeneous line broadening. Such problems arise, for instance, because several radical species or different magnetic sites of rather similar g-values are present or the small **g**-tensor anisotropy of the paramagnetic system does not allow canonical orientations of the powder EPR spectrum to be observed. For improving the spectral resolution by high-field EPR, we have to define a lower limit of the microwave frequency and the corresponding magnetic field $\mathbf{B}_0$. For 'true' high-field EPR experiments, properties of the spectrometer have to be related with properties of the sample: For all cases of delocalized spin systems, in which unresolved hyperfine interactions dominate the inhomogeneous EPR linewidth, a true high-field experiment must fulfill the condition

$$\frac{\Delta g}{g_{iso}} \cdot B_0 > \Delta B \quad (2)$$

i.e. the anisotropic electron Zeeman interaction, described by the difference Δg of principal **g**-tensor components, must exceed the EPR inhomogeneous linewidth ΔB. Figure 1(a) demonstrates the dramatic gain in resolution by increasing the microwave frequency and $\mathbf{B}_0$ field from conventional X-band (9.5 GHz) to W-band (95 GHz) and up to 360 GHz, provided ΔB is not significantly enlarged by relaxation and/or 'g-strain' effects (see following text).

On the other hand, when ΔB is reduced by isotope labeling, e.g. by perdeuteration of the nitroxide spin-label molecule and/or ^{14}N-substitution by ^{15}N, lower B_0 fields maybe already sufficient to meet the condition for true high-field EPR; Eqn (2). This is demonstrated in Fig. 1(b) with 95-GHz EPR on unbound MTS spin label (MTSSL) (see following text) in its protonated, perdeuterated and ^{15}N-substituted/perdeuterated forms.

Moreover, the reduction of ΔB by isotope labeling may turn out to be the only way to enhance spectral resolution, namely, in situations when linearly field-dependent 'g-strain' effects[13] become the linewidth-determining factor at high Zeeman fields and correspondingly high microwave frequencies (Fig. 2). The g-strain line broadening is caused by a spread in the principal g-values as a result of random or discrete local strains exerted on the paramagnetic centers in the sample.[13] As such, g-strain broadening contains information on g-value distributions, and it is typically exploited in EPR spectroscopy on transition-ion complexes and metallo-proteins with their pronounced **g**-tensor anisotropy. For organic radicals, however, the g-anisotropy is much smaller and, hence, g-strain effects on the linewidth become dominant only at high enough Zeeman fields. In this situation, which applies also to the present

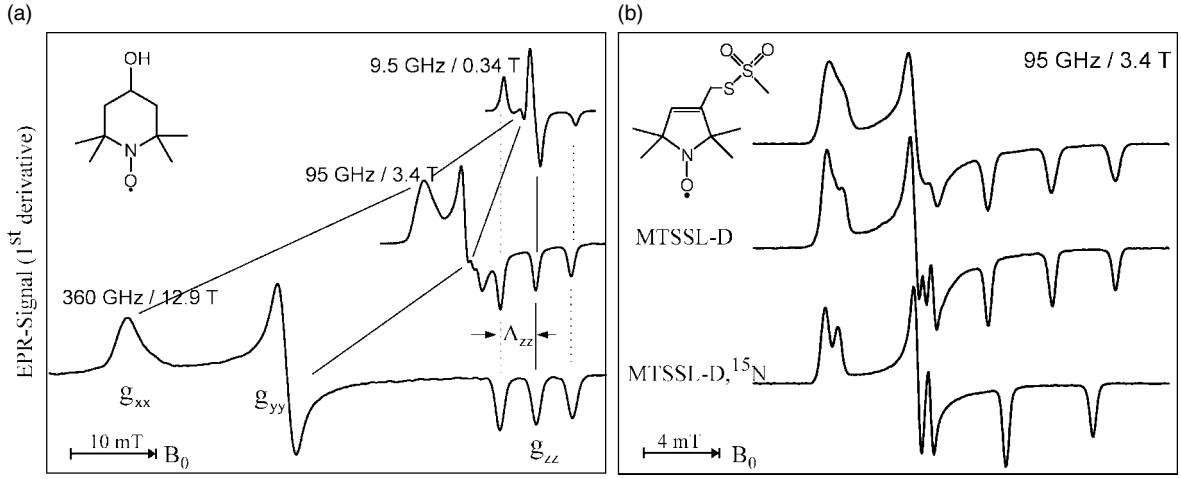

Figure 1. (a) First-derivative cw EPR spectra of a nitroxide radical (OH-TEMPO) in frozen water solution at different microwave frequency/B_0 settings. The spectra are plotted relative to the fixed g_{zz}-value. (b) First-derivative cw W-band EPR spectra of unbound MTS spin label (MTSSL) (top), perdeuterated MTSSL-D (middle) and ^{15}N-substituted, perdeuterated MTSSL-D, ^{15}N (bottom) dissolved in *ortho*-terphenyl glass, $T = 180$ K.

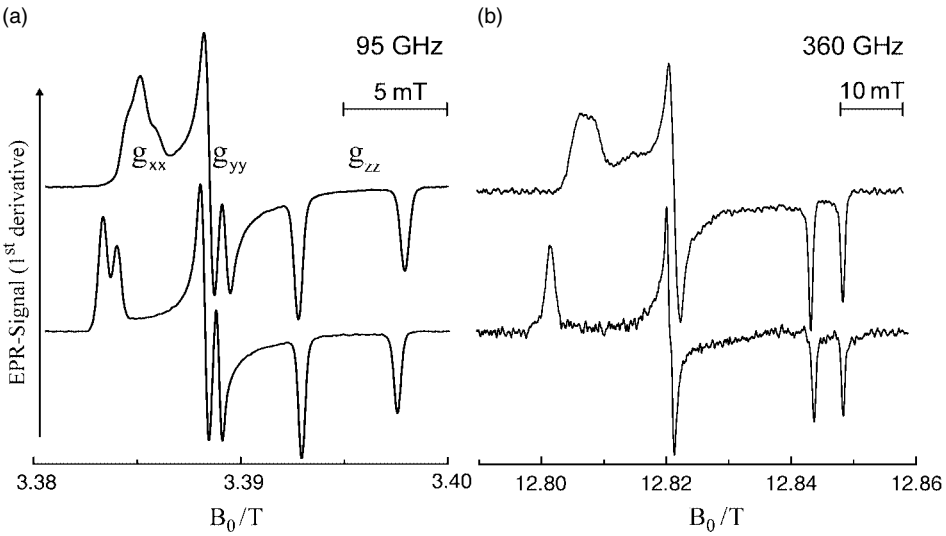

Figure 2. W-band (a) and 360 GHz (b) cw EPR spectra of unbound ^{15}N-,*D*-substituted MTSSL taken at 180 K in frozen solutions of water (upper spectra) and *ortho*-terphenyl (lower spectra). Spin-label concentration was 1 mM. The characteristic doublet hyperfine splittings in the g_{xx}, g_{yy}, g_{zz} spectral regions originate from the ^{15}N nucleus. *Ortho*-terphenyl frozen solution: The linewidth of the EPR lines is almost field independent at 95 GHz. At 360 GHz, however, the g_{xx} spectral region is considerably broadened, as compared to the g_{yy} and g_{zz} regions, due to '*g*-strain' effects. They are attributed to random distributions of nitroxide conformations, as well as small random changes of the local polarity of the microenvironment. Water frozen solution: Because of the large *g*-strain effects typical for frozen water, the g_{xx} spectral region is considerably broadened already at W-band. At 360 GHz, *g*-strain broadening is considerably larger and can be even detected in the g_{yy} region. The *g*-strain is attributed to a local polarity distribution (random), and to proticity (H-bonding) distributions, both random and discrete.

case of nitroxide spin labels, *g*-strain broadening is often an unwanted effect since it may obscure the sensitivity of the g_{xx} tensor component of the spin-carrying moiety for probing local properties of its microenvironment, such as polarity, proticity and pH (see following text). In Fig. 2 it is shown that in the frozen *ortho*-terphenyl solution the ^{15}N-substituted/perdeuterated spin label (abbreviated MTS, see following text) exhibits *g*-strain broadened g_{xx} (and g_{yy}) lines only at an EPR frequency as high as 360 GHz, whereas in the frozen water solution the g_{xx} line is broadened already at 95 GHz.

Some of the important issues for a better understanding of the biological process on the molecular level are (i) the spatial structure of, and the distances and orientations between, cofactors and neighboring protein sections, i.e. the protein topography; (ii) the electronic structure of the cofactors in interaction with their protein microenvironment; (iii) the conformational changes of specific protein segments during biological action, (iv) the hydrophobic barriers for ion transfer along channels in transmembrane proteins; (v) the side-chain accessibility of solvents at specific protein positions; (vi) the polarity and proticity profiles of certain regions of the protein embedded in its amino acid environment; (vii) the molecular dynamics of side chains and potential changes of their mobility during the biological process and (viii) the transient intermediates of the process and their characterization in terms of structure and dynamics.

To provide solutions to such issues, advanced multi-frequency EPR spectroscopy, both in the continuous wave (cw) and pulsed mode of operation, has proven to be very powerful, in particular, when transient paramagnetic states are formed during the biological process. Prominent examples are the light-driven one-electron transfer processes occurring in photosynthesis.

In the case of biological processes that do not involve any stable or transient paramagnetic species or states, such as the light-driven proton transfer in bacteriorhodopsin (BR), EPR can still be used by resorting to artificial paramagnetic probes, termed *spin labels*, introduced into the system, e.g. nitroxide radicals. In this respect, an extremely powerful method for studying the structure and conformational dynamics of proteins under conditions relevant to function has emerged from the pioneering work of Hubbell[14], who had introduced the protocol for site-directed nitroxide spin labeling (SDSL) via position-specific cystein substitution mutagenesis. In SDSL experiments, often the methanethiosulfonate (MTS) spin label (1-oxyl-2,2,5,5-tetramethylpyrroline-3-methyl)methanethiosulfonate is used to take advantage of its sulfhydryl specificity and its small molecular volume, which is rather similar to that of the phenylalanine or tryptophane side chains. In contrast to natural amino acid side chains, however, the MTSSL is not rigidly connected with the protein backbone but linked by a rather flexible tether. This leads to a residual motion of the spin label even when the overall protein motion is frozen at low temperatures. Multi-frequency EPR techniques have been applied in recent years in conjunction with sophisticated lineshape analysis methods, such as those developed by Freed[15] on the basis of the stochastic Liouville formalism to analyze the complex dynamics of spin-labeled protein systems and to separate the spin-label motion from the protein motion at different temperatures,[16] thereby enabling deeper insights into the complex protein dynamics to be revealed.

Spin-label mobility may not necessarily mean a drawback because it allows probing of geometrical constraints of the binding site. However, when the motion of a whole protein segment is of prime interest, e.g. close to the glass transition temperature of the protein, a more rigid attachment of the spin-label to the protein backbone is desirable. In fact, the applicability of the SDSL technique has been considerably expanded very recently by synthesizing and incorporating artificial amino acids with spin-label side chains into the protein at chosen positions.[17] These spin-label amino acids are designed to reduce internal mobility of the label and, hence, to simplify discrimination between protein backbone dynamics and its modulation upon conformational changes during biological function, and residual spin-label side-chain dynamics.[18]

Traditionally, SDSL techniques have been employed in conjunction with standard X-band EPR spectroscopy, and the power of the method in terms of structure determination and sensitivity to reorientational dynamics has been extensively reviewed.[11,19–21] By combining SDSL techniques with high-field/high-frequency EPR however, a new dimension for the SDSL applicability concerning sensitivity and selectivity to molecular motion, to polarity and proticity changes of the microenvironment of the spin-label, and to conformational changes of spin-labeled protein segments has been introduced recently.[22–28]

Additional distinctive strengths of spin-label EPR at high fields and frequencies have emerged that are important for studies of specific biological samples related to this paper: (i) The small g-anisotropies of nitroxides and organic cofactors require higher Zeeman fields than in X-band EPR to resolve all the canonical **g**-tensor components in the slow-motion or powder spectra and, thereby, to enable the tracing of orientation-selective motion and hydrogen bonding in the binding sites. In particular, it is important to resolve the $(g_{xx} - g_{yy})$ anisotropy to analyze nonaxial interactions and motions. (ii) Different sites and orientations of attached spin labels can be separated by means of their small differences in their **g**- and hyperfine tensor interactions. (iii) High-field/high-frequency EPR spectrometers dedicated to (bio)chemical applications can reach high detection sensitivity and time resolution well beyond those at X-band. This is essential for protein systems that can only be prepared in minute quantities. (iv) High-field/high-frequency cw EPR generally provides, by lineshape analysis, shorter time windows than X-band EPR down into the picosecond range, i.e. it is more sensitive to rapid internal motions and allows short correlation times of protein folding and reorientation to be measured over large temperature ranges, while slower motions are already within the rigid limit. For more details about the extraordinary features of high-field/high-frequency EPR and ENDOR (electron–nuclear double resonance) spectroscopy, we refer to overview articles, for example.[9,10,12,15,26,27,29–39]

In this paper, our main object is twofold: (i) to review our recent spin-label high-field EPR work on paradigmatic transfer proteins, such as the BR light-driven proton pump and the Colicin A ion-channel forming bacterial toxin, to obtain new insights concerning the molecular mechanisms of their biological activity, and (ii) to briefly report on novel high-field EPR experiments for probing site-specific, i.e. local pK_a values in protein systems by means of pH-sensitive nitroxide spin labels. Part (i) focuses on proton-transfer intermediates of selectively MTS-labeled BR mutants from *Halobacterium salinarium* to determine potential barriers and molecular switches for the vectorial transmembrane proton transfer. Furthermore, in this part, the high-field EPR results on the refolding intermediates of selectively MTS-labeled mutants of the channel-forming protein domain of Colicin A bacterial toxin produced in *Escherichia coli* are reviewed. Part (ii) gives a preliminary account of potentials and limitations of pH-sensitive SDSL techniques in conjunction with high-field EPR for elucidating complex biological ion-transfer processes that are accompanied by transient local changes of proton availability. The paper concludes with an outlook of ongoing 95-GHz high-field experiments on singly and doubly spin-labeled proteins, e.g. pulsed double-frequency and field-jump W-band PELDOR (pulsed electron–electron double resonance) experiments with time-resolved detection of changes in interspin distances and relative orientations of two-spin systems as well as of ongoing 360-GHz cw EPR experiments on two-spin systems at low temperatures (FU Berlin). Furthermore, the outlook touches ongoing W-band EPR experiments in Osnabrück on the structure and conformational dynamics of the sensory rhodopsin-transducer membrane protein complex.

EXPERIMENTAL

Most high-field EPR experiments of this publication have been performed with a W-band spectrometer operating in both cw and pulsed modes at an EPR frequency around 95 GHz and an external magnetic field of about 3.4 T. In some cases, even higher Zeeman resolution was desirable, and supplementary cw experiments have been performed with a 360 GHz/14 T spectrometer. Both spectrometers are laboratory built and have been described elsewhere.[34,39] Details on experimental conditions, e.g. sample concentrations and temperatures, are either given in the respective paragraphs and figure captions or in the cited references.

Additional information about the topology of the spin-labeled proteins was obtained by accessibility and mobility measurements of the spin-label side chain via X-band EPR, as has been described previously.[40]

MTSSL was synthesized according to Berliner *et al*.[41] The isotopomers D_{15} as well as the $D_{15}-{}^{15}N_1$ were prepared each in a ten-step synthesis following reactions described in Refs 41 and 42. In order to get a deuteration degree as high as possible (98–99%), the key precursor, triacetonamine-^{15}N-perdeuterated, was synthesized from $^{15}ND_3$ and deuterated acetone. Details of these modified reactions will be published elsewhere.

IMT spin label (IMTSL) (methanethiosulfonic acid *S*-(1-oxyl-2,2,3,5,5-pentamethyl-imidazolin-4-ylmethyl) ester) was synthesized as described in Ref. 43.

Mutagenesis, expression as well as MTS and IMT spin labeling of the proteins were performed as described in Refs 24 and 40 for BR and in Ref. 22 for colicin A.

RESULTS AND DISCUSSION

Bacteriorhodopsin

Nature has invented photosynthesis twice, i.e. the strategy to use sunlight as energy source to synthesize ATP: In the photosynthetic reaction center (RC) protein complex of purple bacteria, this is initiated by light-induced primary *electron* transfer between bacteriochlorophyll and quinone cofactors, mediated by the protein microenvironment. In the BR protein complex, this is set going by light-initiated primary *proton* transfer between amino acid residues, mediated by conformational changes of the only cofactor, the retinal.

BR is a 26 kDa protein complex located in the cell membrane of halophilic archaebacteria such as *H. salinarium*. High-resolution X-ray crystallography coordinates are available for the ground-state structure[44] (Fig. 3). Seven transmembrane helices (A–G) enclose the chromophore retinal that is covalently attached to the amino acid lysine, K216 on helix G, via a protonated Schiff base. Absorption of 570-nm photons initiates the all-*trans* to 13-*cis* photoisomerization of the retinal. The Schiff base then releases a proton to the extracellular medium and is subsequently reprotonated from the cytoplasm. Transient intermediates of this catalytic photocycle can be distinguished by the different absorption properties of the retinal, and a sequence of intermediates, J, K, L, M, N and O, has been characterized by time-resolved absorption spectroscopy.[45] Double-flash experiments revealed that the M intermediate is divided into two substates, M_1 and M_2.[46,47] During this photocycle, conformational changes of the protein (and the retinal) occur, as has been detected by a variety of experimental techniques (for a review, see, e.g. Ref. 48). Such changes ensure that release and uptake of protons do not occur from the same side of the membrane, but rather enable BR to work as a vectorial transmembrane proton pump. To this end, in wild-type BR conformational changes associated with the M_1 to M_2 transition are suggested to function as a 'reprotonation switch' required for the vectorial proton transport. It is believed that during the lifetime of the M state the accessibility of the Schiff base for protons is switched from the extracellular to the cytoplasmic side of the membrane. Detailed analyses of the nature of the conformational changes include neutron diffraction, electron microscopy, X-ray diffraction, solid-state NMR or EPR spectroscopy. The studies reveal that major changes occur at the cytoplasmic moieties of helices F and G. In wild-type BR, such helix movements have been shown to provide an 'opening' of the protein to protons on the cytoplasmic end of the transmembrane proton channel.[49] Thereby, proton transfer can occur from the internal aspartic acid proton donor, D96, to the Schiff base during the M to N transition. The reprotonation of D96 from the cytoplasm occurs during the recovery of the BR initial state. A detailed inspection of the structure of the unilluminated state of the protein reveals that certain amino acid side chains block the proton pathway from the cytoplasm to D96.[49] The region between D96 and the Schiff base is largely nonpolar, packed with bulky amino acid residues. Hence, in this unilluminated state, the Schiff base is effectively inaccessible to protons from the cytoplasm. In the light-driven M_1 to M_2 transition, this region is opened for access of protons to the Schiff-base nitrogen atom. However, the question remains whether the

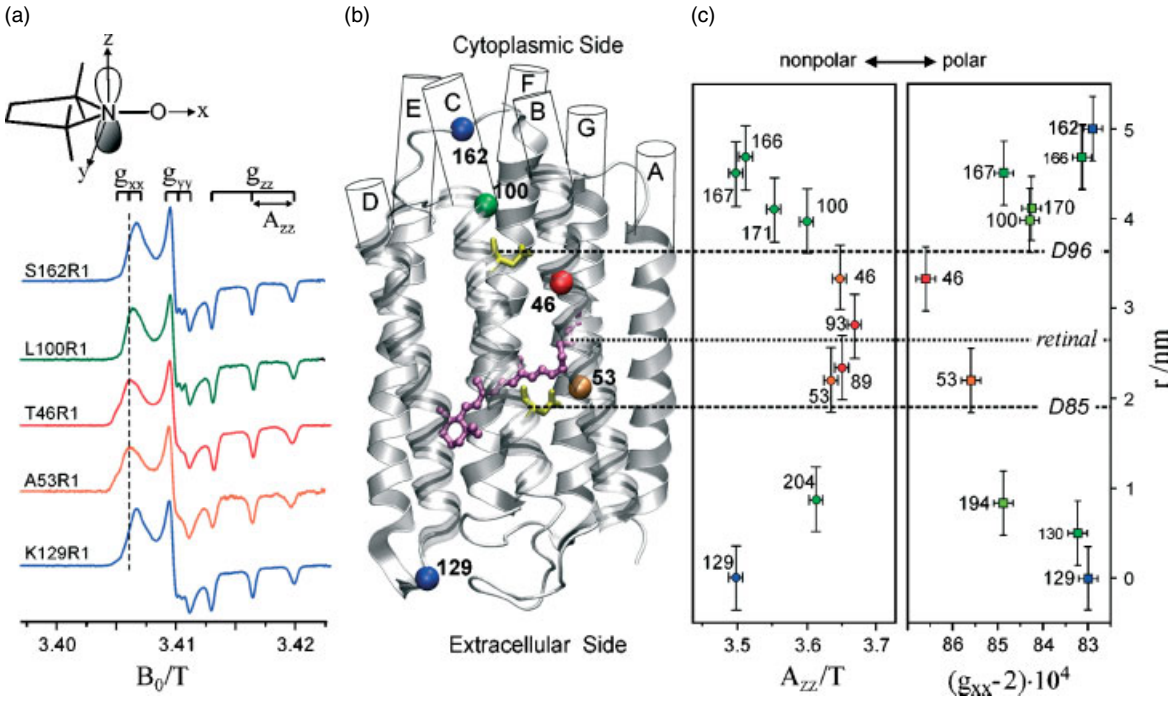

Figure 3. (a) Experimental W-band cw EPR spectra for a set of bacteriorhodopsin (BR) mutants spin-labeled with the MTSSL nitroxide side chain (R1). (b) Structural model of BR. The C_α atom of the spin-labeled residues, seven α-helices A–G, the chromophore retinal and D96 and D85 participating in the H^+ transfer are indicated. (c) The magnitude of the tensor elements A_{zz} and g_{xx} of the spin labels are plotted as function of the nitroxide location in the protein with respect to position 129. For details, see Ref. 24.

relatively large conformational changes observed in the photocycle of the wild-type BR and many BR mutants are a prerequisite for vectorial proton transport, i.e. if they really represent the proposed reprotonation switch.

Obviously, additional spectroscopic experiments are needed on wild-type BR and strategically constructed BR mutants to follow even small, but significant, conformational changes of protein and cofactor during the photocycle. In this respect, the combination of site-directed mutagenesis for spin labeling and high-field EPR for resolving structural changes of proteins at work is particularly powerful. It provides – in addition to the nitrogen hyperfine tensor component A_{zz} – the resolved **g**-tensor components g_{xx}, g_{yy}, g_{zz} as sensitive probes for studying conformational changes of the labeled protein segment and interactions with the microenvironment, e.g. polarity and hydrogen-bonding effects (Fig. 3 shows the molecular axes system chosen for the nitroxide fragment).

As was shown in Fig. 1, a remarkable gain in resolution of nitroxide-radical spectra, i.e. the separation of the g_{xx}, g_{yy}, g_{zz} components in relation to the A_{zz} hyperfine splitting is achieved when increasing the Zeeman field from X-band EPR to 95- and 360-GHz EPR. For our systematic studies, a set of SDSL mutants was constructed, each containing a single nitroxide side chain, differing by position in the protein sequence. The photocycle of all spin-labeled mutants was checked to ensure that the overall function of the BR protein is retained.[23,24]

Hydrophobic barrier of the BR proton-transfer channel

By 95-GHz high-field EPR details of the polarity profile along the putative proton channel were probed by **g**- and hyperfine tensor components from a series of 10 site-specifically nitroxide spin-labeled BR mutants, with MTSSL as the reporter side chain R1.[23] Previous studies of a large number of spin-labeled proteins have shown that the A_{zz} component of the ^{14}N hyperfine tensor and the g_{xx} component of the **g**-tensor are particularly sensitive probes of the microenvironment of the NO$^{\bullet}$ side chain R1. They allow the measurement of changes in polarity and proticity, i.e. g_{xx} and A_{zz} probe the local electric fields and the availability of H-bond forming partners of nearby amino acid residues or water molecules.[23–25] Moreover, the dynamic properties of the NO$^{\bullet}$ side chain and, thus, the EPR spectral lineshape have been shown to contain direct information about constraints to motion that are introduced by the secondary and tertiary structures of the protein in the vicinity of the nitroxide binding site.[23,24]

For measuring the polarity changes, W-band EPR spectra were recorded at temperatures below 200 K to avoid motional averaging of the anisotropic magnetic tensors. At these temperatures, R1 can be considered as immobilized on the EPR timescale. The spectra of selected mutants are shown in Fig. 3. They exhibit the typical nitroxide powder-pattern lineshape expected for an isotropic distribution of diluted radicals. The variations of g_{xx} and A_{zz} with the nitroxide binding site can be measured with high precision, and plots of g_{xx} and A_{zz} vs R1 positions along the proton channel directly reflect the hydrophobic barrier that the proton has to overcome on its way through the protein channel (Fig. 3).

The analysis of both tensor components, g_{xx} and A_{zz}, enables to characterize the R1 environment in terms of *protic* and *aprotic* surroundings. Theoretically, both g_{xx} and A_{zz} are expected to be linearly dependent on the π-spin density $\rho_\pi{}^{O}$ at the oxygen atom of the nitroxide group. The hyperfine component A_{zz}, given by[25]

$$A_{zz} = Q_\pi^N \cdot \rho_\pi^N \tag{3}$$

is linearly dependent on $\rho_\pi{}^{O}$ on account of the sum condition $\rho_\pi{}^{O} + \rho_\pi{}^{N} \cong 1$. For g_{xx}, however, apart from a direct proportionality to $\rho_\pi{}^{O}$, there is an additional dependence on specific properties of the oxygen lone-pair orbitals. This follows from an approximate expression for g_{xx} derived by Stone[50–52] for organic π-radicals:

$$g_{xx} \cong g_e + \frac{2 \cdot \zeta(O) \cdot \rho_\pi^O \cdot c_{ny}^2}{\Delta E_{n\pi^*}} \tag{4}$$

where $g_e = 2.0023$ is the free-electron g-value; $\zeta(O)$ is the oxygen spin-orbit coupling parameter; $\rho_\pi{}^{O}$ is the π spin density on the oxygen $2p_z$ atomic orbital; c_{ny} is the LCAO coefficient of the $2p_y$ atomic orbital contributing to the oxygen lone-pair MO; and $E_{n\pi*}$ is the $n \rightarrow \pi^*$ excitation energy.

The lone-pair orbital energy E_n affects g_{xx} via the excitation energy $\Delta E_{n\pi^*} = E_{\pi^*} - E_n$ and is known to be sensitive to the electrostatics, i.e. the polarity of the environment. This effect adds to the polarity dependence of $\rho_\pi{}^{O}$ on account of the charge displacements in the NO π-bond. E_n is particularly sensitive to H bonding of the lone pairs to water or to polar amino acid residues in the surrounding medium. Furthermore, H bonding can also affect the partial electron population c_{ny}^2 of the lone-pair orbitals.

Thus, any change $\delta\Delta g_{xx}$ in $\Delta g_{xx} = g_{xx} - g_e$ can be broken down into three contributions:

$$\frac{\delta\Delta g_{xx}}{\Delta g_{xx}} \cong -\frac{\rho_\pi^N}{\rho_\pi^O} \cdot \frac{\delta A_{zz}}{A_{zz}} - \frac{\delta\Delta E_{n\pi^*}}{\Delta E_{n\pi^*}} + \frac{\delta c_{ny}^2}{c_{ny}^2} \tag{5}$$

Qualitatively, Eqn (5) correctly predicts the observed negative slope of the g_{xx} vs A_{zz} plot. The last two terms are responsible for additional vertical deviations.

In the next step, a quantitative treatment of polarity and H-bonding effects was attempted. Following Griffith *et al.*,[53] polarity effects from the various intermolecular electric fields originating in dispersion forces, permanent electric dipole interactions, induced dipole interactions etc. are most conveniently described by a single collective parameter, the average local electric field $\boldsymbol{E}$ in the NO bond region.[53] These authors show that the π spin density at the nitrogen atom, ρ_π^N, changes to first order as

$$\delta\rho_\pi^N = C_1 \cdot E_x \tag{6}$$

where E_x is the electric field component along the NO bond and $C_1 \cong 2 \cdot 10^{-9}$ V^{-1} cm.[53] Regarding the observed maximum change of A_{zz} of 0.4 mT and applying Eqn (3), Eqn (6) predicts an effective 'polarity range' $0 < E_x \leq 2 \cdot 10^7$ V cm^{-1} for the MTSSL at the different sites in BR. Thus, in our calculations, we imposed a uniform electric field E_x

in a nitroxide spin-label model system as effective polarity parameter, applying values of E_x that cover this polarity range. This was achieved by using the electric field setup options within the molecular modeling package Hyperchem (Hypercube Inc., Gainesville FL, USA).

Effects of H bonding (hb) on the g_{xx} vs A_{zz} dependence have been studied theoretically on a nitroxide model structure (inset of Fig. 4(a)) with one water molecule H bonded to the O atom. Our approach was similar to that of a theoretical study on tyrosyl radicals.[54] Fig. 4(a) shows the calculated g_{xx} vs A_{zz} dependence for this nitroxide spin-label model. For the quantum-chemical method (ZINDO/S) used for calculating the various quantities determining g_{xx} and A_{zz}, and for further details, see Ref. 25.

The upper dashed line in Fig. 4(a), defined as 'aprotic', is based on the calculated g_{xx} values *without* hb formation, and the lower dashed line is *with* hb formation. This latter line is shifted against the aprotic line by a constant value of -4×10^{-4} over the whole range of E_x values between 0 and 0.02 au (1 au $= 5 \times 10^9$ V cm^{-1}). The solid line, defined as 'protic' in analogy with earlier work,[55] is obtained by linear interpolation between points A and B, which are characterized by the nonpolar/aprotic limit with the experimental value $A_{zz} = 3.36$ mT, and by the highly polar/protic situation in water for which a value $A_{zz} = 3.64$ mT was measured.[25] Both limiting values of A_{zz} could be theoretically reproduced,[25] and the molecular parameters obtained from these calculations where, in turn, used in the calculations of the limiting values of g_{xx} to provide points A and B in Fig. 4(a).

For comparison, experimental results for spin-labeled BR are given in Fig. 4(b). It shows the g_{xx} vs A_{zz} dependence for various spin-label protein positions.[23] Obviously, two straight-line correlations can be deduced in accordance with the theoretical predictions. The points corresponding to positions 46, 171 and 167 belong to a line whose slope is significantly different from that for the remaining points. These three positions can be classified to be exposed to an aprotic environment,[53,55] the other ones to a protic environment. Admittedly, there remains a discrepancy between calculated and experimental slopes of the g_{xx} vs A_{zz} plots.[25] As in earlier studies,[56] it is anticipated that sterically induced strains on the attached nitroxide spin label may influence the slopes dg_{xx}/dA_{zz} and explain the discrepancy. Hence, structural changes of the nitroxide label by superimposed local fields were theoretically analyzed as a possible reason for the striking difference between calculated and measured slopes.[25] Indeed, the analysis shows[25] that 'polarity induced steric strain' results in deviations from planarity of the label skeleton which, in turn, reduce the calculated slope dg_{xx}/dA_{zz} – via combined action of energy and spin density changes – toward the experimental value (for details of the calculations, see Ref. 25). In conclusion, it is justified to state that the g_{xx} vs A_{zz} plot enables the hydrophobic barrier of the BR proton channel to be characterized in terms of different accessibilities of the respective protein regions to water molecules. The discussed sensitivity of the resolved g_{xx} and A_{zz} tensor components of nitroxide radicals to the polarity of their microenvironment has been recognized also by other high-field EPR research

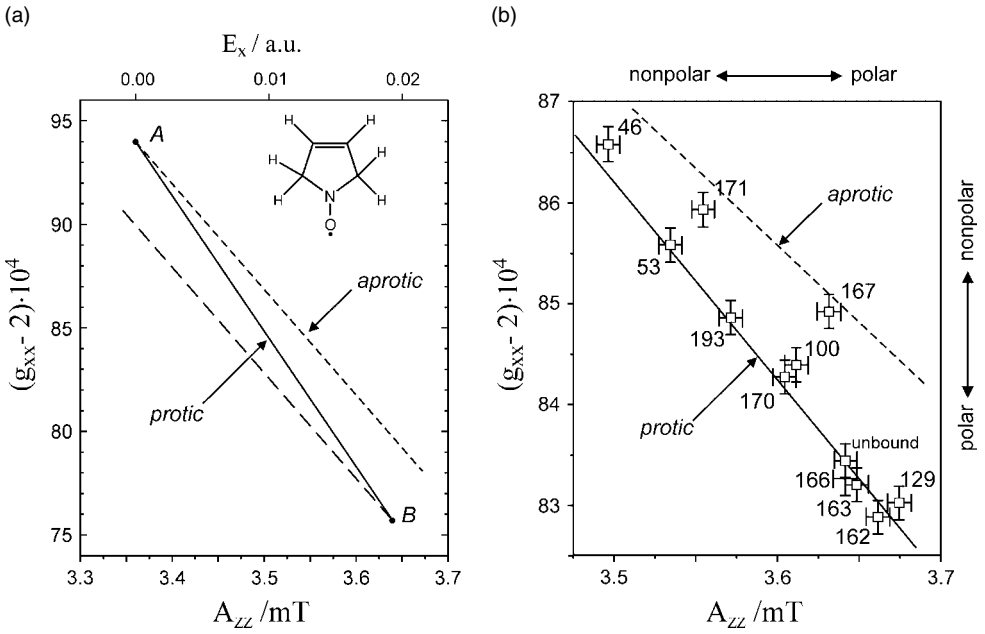

Figure 4. (a) Theoretical plot of g_{xx} vs A_{zz} for a planar nitroxide model radical as calculated for the 'aprotic' case (without hydrogen bonding, short dashes) and for the case with additional hydrogen bonding (long dashes). The 'protic' line (solid line) is obtained by linear interpolation between the nonpolar limit (point A, $A_{zz} = 3.36$ mT) and the water limit (point B, $A_{zz} = 3.64$ mT). For details, see text and Ref. 25. (b) Experimental plot of g_{xx} vs A_{zz} of the nitroxide side chains for various spin-label positions in bacteriorhodopsin (see text). The 'protic' and 'aprotic' limiting cases are derived in analogy with corresponding theoretical lines; see left side of this figure. The absolute *g*-values as well as the slopes of the 'protic' and 'aprotic' lines are different from the results of model calculations. This discrepancy is discussed in the text; for more details, see Refs 23 and 25.

groups, e.g. for nitroxide spin labels in frozen solutions[57] and phospholipid membranes.[12,37,56]

Conformational changes during the BR photocycle

The discussion about conformational changes of distinct helices in BR to activate a molecular switch for vectorial proton transfer has been revived recently by the investigation of the tailor-made triple mutant D96G/F171C/F219L that modifies the cytoplasmic proton entrance region, Fig. 5(a). This BR triple mutant reveals a remarkable conformation of its dark state: It was shown to resemble that of the late M intermediate (preceding N in the photocycle) in wild-type BR, but with a conformation that is retained upon illumination (*pseudo* M state).[24,49,58,59] In our work, the triple mutant was MTS labeled and studied by W-band high-field EPR without and with light irradiation.[24] The goal was to test the sensitivity of selectively spin-labeled helix segments in singly, doubly and triply mutated BR toward changes of the microenvironment in the cytoplasmic region during the photocycle. In these studies, we chose position 171 at the cytoplasmic end of helix F (Fig. 5(a)) in the single mutant F171C, in the double mutant D96G/F171C, and in the triple mutant D96G/F171C/F219L for attaching an MTSSL to the unique cysteine, thus forming the side chain R1. The R1 probe is used to measure the polarity changes in this region via light-induced shifts of the g_{xx} and A_{zz} tensor components. The results are depicted in Fig. 5(b). It nicely shows that upon light excitation of the single mutant to its M state, the NO• residue at position 171 experiences the same nonpolar microenvironment as the triple mutant with its *pseudo* M state open for proton uptake already in the dark.[24]

Pronounced conformational changes of wild-type BR during the photocycle were also observed in the high-field EPR spectra of selectively spin-labeled double mutants D96N/V167R1 and D96N/V101R1 in their ground states recorded in the dark and under light illumination. The dark-minus-light spectra clearly show an *increased* reorientation mobility of the nitroxide side chain R1 in the M intermediate of the D96N/V161R1 mutant, but a *decreased* mobility for D96N/V101R1. Obviously, the residual anisotropy of the nitroxide motion changes during the photocycle owing to changing space restrictions within the R1 binding site. Label V167R1 is located at the cytoplasmic moiety of helix F and oriented toward helix C. Thus, an increase of the interhelical distance, caused by displacement of helix F or helix C, would account for the experimental data – in accordance with neutron-diffraction and FT-IR results and with EPR interspin distance measurements of doubly labeled BR variants[60] (for details, see Ref. 23).

Colicin A bacterial toxin

Colicin A is a member of a family of bacterial toxins that form transmembrane ion channels.[61–63] They are water-soluble proteins, mostly about 70 kD in size, and have varying homology among themselves. Colicin A kills unprotected cells of attacked organisms by inserting specific segments of protein subdomains into the cytoplasmic membrane forming a voltage-gated ion channel. The open channel leads to electrical depolarization of the membrane and depletion of intracellular ion pools, which ultimately leads to cell death. An understanding of these mechanisms on the molecular level is currently also of biomedical interest, since insertion of proteins into membranes and subsequent channel formation

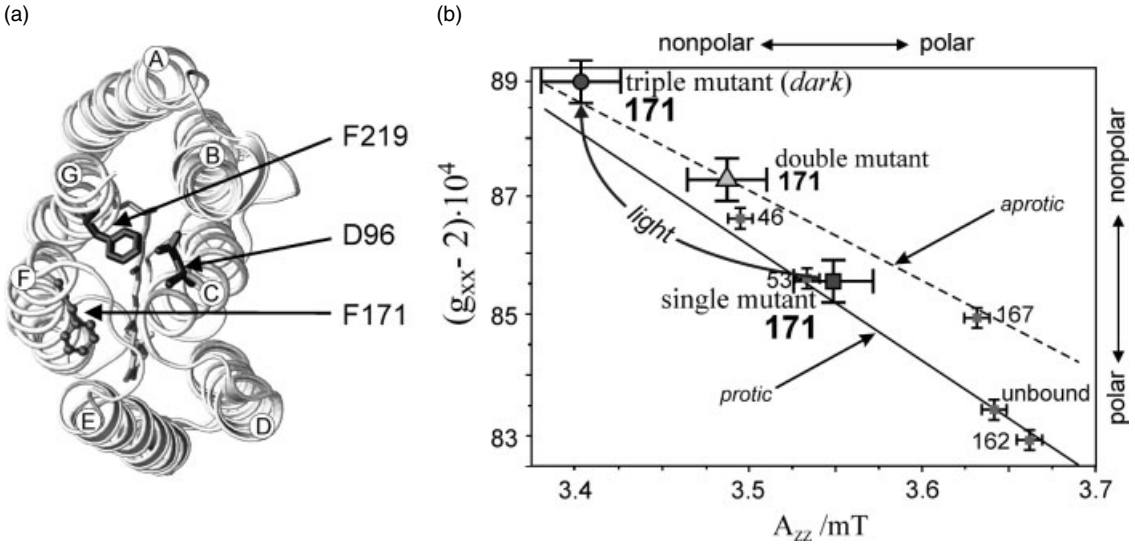

Figure 5. (a) Top view of the X-ray structural model of bacteriorhodopsin.[49] The seven α-helices (A–G) and the interconnecting loops are visible as well as positions D96, F171 and F219 in their nonmutated forms are shown. (b) Polarity plot of g_{xx} vs A_{zz} of the nitroxide side chains R1 for various spin-label positions in BR mutants with emphasis on the R1 position 171 in the single mutant F171R1 (square), the double mutant D96G/F171R1 (triangle) and the triple mutant D96G/F171R1/F219L (circle). The dark state of the triple mutant reveals a very nonpolar protein microenvironment of R1 in the vicinity of the cytoplasmic entrance of the proton channel. Light excitation of the single mutant switches the microenvironment of R1 to the same nonpolar properties as experienced by the triple mutant in the dark (the g_{xx}, A_{zz} data points of the single mutant F171R1 in the light state coincide with those of the triple mutant in the dark state). For details, see Refs 24 and 59.

are common to many toxic proteins of bacterial pathogens, such as the diphtheria, tetanus and cholera toxins.[62–66]

The colicin toxins have to overcome the protecting barriers of the attacked cell.[61,67] Accordingly, Colicin A consists of three functional protein domains: The central receptor domain R, the *N*-terminal translocation domain T to penetrate the outer membrane and to traverse the periplasm, and the *C*-terminal channel-forming domain C to penetrate the inner membrane that protects the cytoplasm of the cell.[63,68] These distinct functions of the colicins are reflected by their three-dimensional shape. The X-ray crystal structure of a complete (T-R-C) Colicin Ia protein was recently determined to 2.3 Å resolution.[63,69] It reveals a harpoon-shaped molecule, 210 Å long, with the three functional domains well separated from each other to overcome the protection barriers of the attacked cell.

The isolated C-domain retains its channel-forming ability in aqueous solutions of artificial membranes[70,71] such as lipid vesicles. Hence, details of refolding processes of the C-domain can be studied by *in vitro* experiments (see following text). The X-ray crystal structure of the 204-residue (21 kD) channel-forming C-domain of Colicin A in its water-soluble conformation is available to 2.4 Å resolution.[72] Ten α-helices, eight amphiphilic, two hydrophobic, are arranged in such a way that the amphiphilic helices surround the hydrophobic hairpin (helices 8 and 9), which is deeply buried in the center of the protein (Figs 6 and 7(a)). Thereby, the hairpin is shielded from contact with the water solvent.

In view of the difficulties encountered in determining X-ray structures of transient proteins in action, numerous spectroscopic techniques are being used to study colicins on the molecular level. Despite many years of work, including EPR studies,[67,74,75] the details of the refolding processes upon membrane association and channel formation are not yet known. Since Colicin A is now so well characterized, it may serve as a paradigm system to answer an intriguing question of general interest in molecular biology and medicine: what is the mechanism to switch on the insertion of water-soluble pore-forming proteins into the nonpolar lipid region of the membrane?

Models of transmembrane ion-channel formation

The C-domain of Colicin A (and other members of the colicin family) can adopt two conformations, the water-soluble form and the transmembrane form. The transition between these conformations requires massive refolding of the tertiary structure. To date, two alternative models are being discussed to explain how the C-domain turns itself inside out to form the membrane-associated state with pore formation, the 'umbrella' model[72] and the 'penknife' model[5] (Fig. 6). Conceptually, they differ in the description of the relatively slow (100 ms–s range) membrane-insertion step to be either spontaneous or voltage dependent. After docking to the membrane surface, a slow, but still voltage-independent refolding of the C-domain occurs to bring the hydrophobic helices 8 and 9 to the outside of the protein complex. In the umbrella model, the hydrophobic hairpin spontaneously traverses the membrane, whereas in the penknife model, the refolding leaves the hairpin close to the membrane surface, but a change of the electric transmembrane potential is required to trigger insertion of the hairpin into the membrane and, ultimately, to open the channel for ion flow.

W-band EPR on membrane-insertion mechanisms

In our work on Colicin A transient states, we applied high-field EPR at 95 GHz in conjunction with site-directed

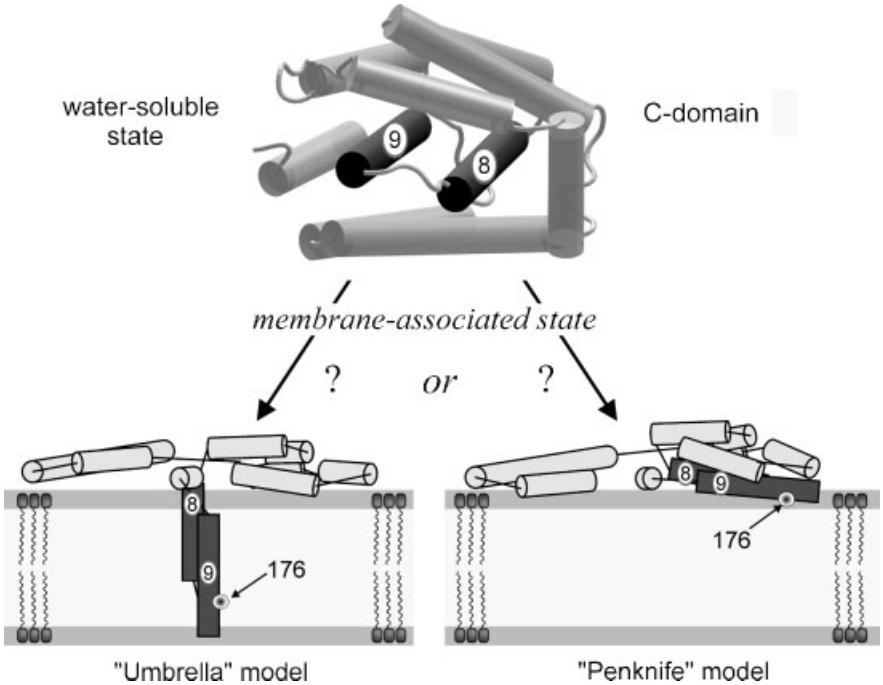

Figure 6. The 'umbrella' model[72] and the 'penknife' model[5] of the membrane-associated state of the channel-forming C-domain of Colicin A. In the water-soluble state of the C-domain, the hydrophobic helices 8 and 9 are deeply buried in the interior of the domain where a nonpolar microenvironment is energetically stabilized.

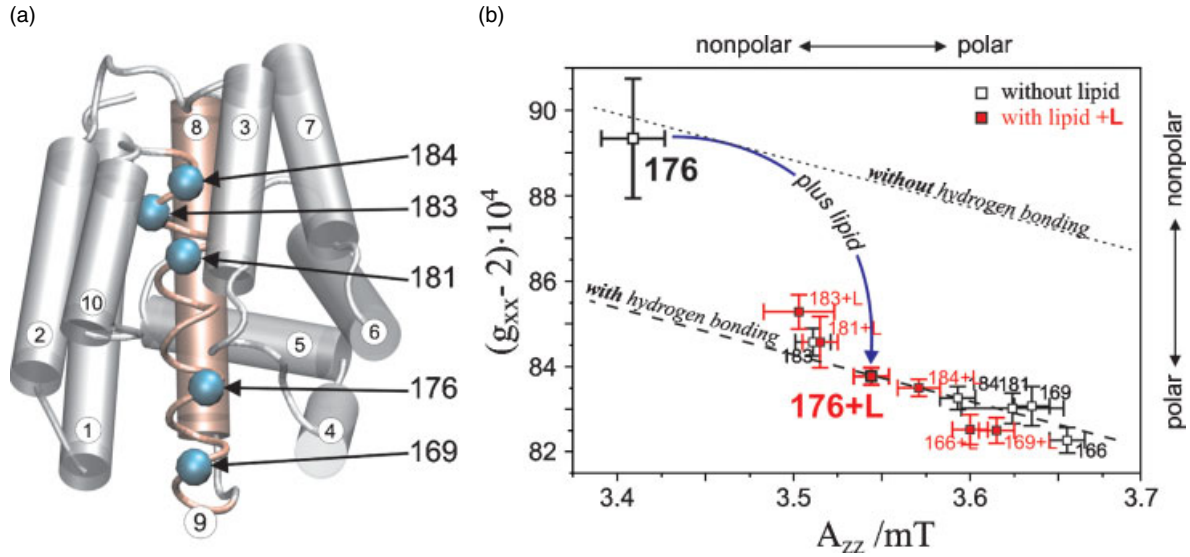

Figure 7. (a) X-ray structural model (side view) of the channel-forming C-domain of Colicin A. The positions of cysteine replacements in helix 9 by site-directed exchange mutagenesis are indicated by numbered spheres (169, 176, 181, 183, 184). The α-helices are labeled 1 (*N*-terminus) to 10 (*C*-terminus). The hydrophobic helices are 8 and 9. For details, see Refs. 5, 72 and 73. (b) Polarity plot of g_{xx} vs A_{zz} for the nitroxide spin-label positions in helix 9 of site-directed Colicin A mutants. The measured tensor components with addition of lipid vesicles and without lipid addition are marked by full and open squares, respectively. The dashed lines define the limits between the nonhydrogen bonded (short dashes) and the fully hydrogen bonded (long dashes) cases (Fig. 4). For details, see Refs. 22, 23 and 25.

MTS spin-labeling techniques.[22] Owing to the high spectral resolution achieved by 95-GHz EPR, we could use both the A_{zz} hyperfine tensor component of the ^{14}N nucleus and the g_{xx} tensor component as sensitive probes for the polarity and proticity of the microenvironment of the nitroxide side chain R1 and for its motional characteristics in three-dimensional space under the local constraints of the protein.[24,25]

In Fig. 7(a), the five individual amino acid residues of helix 9 of the C-domain that have been replaced by cysteines via exchange mutagenesis[5,73] at positions 169, 176, 181, 183 and 184, respectively are indicated by numbered spheres. Subsequently, the single cysteines were spin labeled with MTS. Our experimental strategy for detecting the refolding of the C-domain under membrane association was to compare the EPR spectra of Colicin A in buffered aqueous solution under physiological conditions (pH 8) with those after adding lipids to the sample to form vesicles as artificial membranes.[22] To this end, small unilamellar vesicles were made by sonification of the sample containing the lipid DMPG (1,2-dimyristoyl-*sn*-glycero-3-phospho-*rac*-(1-glycerol)) in water.

The tensor components A_{zz} and g_{xx} were measured for the five mutants.[22] In the water-soluble conformation (no lipid added), the A_{zz} and g_{xx} values reveal high polarity at the water-accessible sites of helix 9 (positions 184, 169), and a lower polarity in the protected center (position 176). This finding is consistent with the amino acid configuration known from the X-ray crystal structure.[72] After addition of lipid, a rather uniform, high-polarity character of the nitroxide microenvironment of all mutants results. The highest polarity change is experienced by R1 attached to position 176 in the central part of the helix 9.

In Fig. 7(b), the W-band measurements of g_{xx} and A_{zz} are summarized in the plot g_{xx} vs A_{zz}. Both probes show that the central-region position 176 experiences a strong change in polarity of the microenvironment toward more polar character, whereas in the vicinity of the end-region positions 169, 184, only weak polarity changes occur upon adding lipids.

According to the umbrella model, helices 8 and 9 should penetrate the membrane spontaneously so that their central part, as probed by the nitroxide at position 176 in helix 9, would be placed into the interior of the membrane, i.e. in a highly nonpolar region. This means that in the umbrella model one would expect, for the spin-label at position 176, no large changes of g_{xx} and A_{zz} upon adding lipid to the aqueous sample because, in both states, water-soluble and membrane-associated, the microenvironment would remain nonpolar. According to the penknife model, however, helix 9 should remain for some time in a transient state close to the membrane surface – until an electric potential change initiates helix insertion and pore formation in the membrane. In this situation, R1 at position 176 would experience a drastic change of the microenvironment from nonpolar to polar in the membrane-associated state. This is exactly what we observe by means of the polarity probes g_{xx} and A_{zz} when adding vesicle-forming lipids to the aqueous sample. Hence, our data validate the penknife model for membrane association of the Colicin A channel-forming domain. This conclusion is in agreement with FRET experiments on Colicin A double mutants with site-specifically attached fluorescence labels[5] (for more details, see Ref. 22).

Probing local pK_a effects by pH-sensitive spin labels

As has been shown above, nitroxide radicals can be successfully used to probe the polarity of the microenvironment owing to the sensitivity of the nitroxide EPR parameters to the local electric field, Eqn (6). This electric field may, however, not only originate in the environment of the probe but may also stem from the nitroxide radical itself if it contains ionizable groups. Such compounds have been established as pH-sensitive nitroxide EPR probes,[76] in which pH changes of the bulk solution induce changes of the internal ion state. From the numerous ionizable nitroxides, the imidazoline as well as imidazolidine radicals are considered to be most suitable for biological applications owing to their high stability. Moreover, they exhibit a reversible pH effect, i.e. a reversible protonation of the tertiary amine nitrogen N-3 in the radical heterocycle. Since first reported by Khramtsov and coworkers[77] in 1982, these nitroxides have found a wide application as probes for measuring pH in chemical and biological systems, even when performing *in vivo* experiments.[76] However, up to now, reported studies have employed the pH-sensitive nitroxides either in the free, i.e. unbound form or as a label rather unspecifically attached to the molecule under study.

Recently, Smirnov *et al.*[43] reported a first W-band EPR study of the pH-sensitive nitroxide methanethiosulfonic acid *S*-(1-oxyl-2,2,3,5,5-pentamethyl-imidazolin-4-ylmethyl) ester, IMTSL. This is an imidazolidine derivative of the MTSSL (Fig. 9(c)) and is principally suitable for side-directed spin labeling. The authors performed EPR measurements at room temperature and analyzed the isotropic *g*- and hyperfine values as function on the pH value of water-buffer solutions. However, their results are hardly applicable to spin-labeled proteins, because the nitroxide spin label attached to the protein is normally partially, or even fully, immobilized at room temperature (Fig. 10(a)). Therefore, we performed X- and W-band measurements on IMTSL in liquid as well as in frozen solutions at different pH values with the primary goal of applying this spin label for investigating the local pH value at the D96 proton-donor position of BR and changes of this value during the photocycle.[78]

Significant differences between the IMTSL EPR spectra were observed, both in X-band (Fig. 8(a)) and in W-band (Fig. 8(b)) when varying the pH value of liquid water-buffer solutions between 1.3 and 7.2. The X-band spectra show small shifts of the EPR line position in the motionally narrowed three-line nitroxide spectrum typical for fast-exchange conditions (Fig. 8(a)). The analysis of the isotropic hyperfine coupling A_N, measured as the distance between the central and the high-field lines of the triplet, in terms of the Henderson–Hasselbalch equation[79], yields p$K_a = 2.19 \pm 0.09$ and A_N values of 1.43 mT and 1.58 mT for the protonated (RH^+) and unprotonated forms (R) of IMTSL, respectively (Fig. 8(c)).

In contrast to X-band, at W-band the fast-exchange condition is no longer valid, and the W-band EPR spectra consist of two partially resolved nitroxide triplets at pH values close to pK_a; see line shoulders at pH = 2.5 in Fig. 8(b). Attempts to fit the overall lineshape by simply superimposing the spectra from the fully protonated and the unprotonated form of the spin labels failed. This indicates that the exchange rate between RH^+ and R is comparable in magnitude with the spectral separation of W-band EPR lines of RH^+ and R, i.e. the intermediate-exchange regime prevails. Hence, we analyzed the experimental W-band spectra in terms of modified Bloch equations that include chemical exchange between the protonated and unprotonated form of IMTSL.[80] The EPR spectra, S(B), were calculated using the known analytical expression for EPR absorption. It is given by the imaginary part of the complex magnetization; see Eqn (11) in Chapter 12 of Ref. 80, which was adapted to the nitroxide case by extending it for the three pairs of exchange-coupled ^{14}N hyperfine lines ($m_I = -1, 0, 1 \equiv m$ in the following):

$$S(B)_{RH+,R} \propto \mathrm{Im}\left\{\sum_{m=-1,0,1} \frac{\begin{array}{c} f_{RH+}\cdot(B_{RH+,m}-B)+f_R\cdot(B_{R,m}-B)+ \\ \mathrm{i}(P_{RH+}+P_R) \end{array}}{\begin{array}{c} ((B_{R,m}-B)+\mathrm{i}P_{RH+})\cdot((B_{R,m}-B)+\mathrm{i}P_R)+ \\ P_{RH+}\cdot P_R \end{array}}\right\} \tag{7}$$

where $B_{(RH+,R),m} = B_{0(RH+,R),m} + \mathrm{i}\Delta B_{(RH+,R),m}$. The positions of the individual hyperfine lines, $B_{0(RH+,R),m}$, and their widths, $\Delta B_{(RH+,R),m}$, were determined from the EPR spectra of radicals RH^+ and R. These parameters were kept fixed at further calculations of intermediate exchange. The parameters P_{RH+} and P_R are the effective exchange rate constants rescaled from frequency to field dimension by the factor $(1/\gamma_e)$. They determine also the fraction coefficients $f_{RH+} = P_R/(P_R + P_{RH+})$ and $f_R = P_{RH+}/(P_R + P_{RH+})$ of protonated and unprotonated forms of the spin-label. Because of the relation $P_R = P_{RH+} \cdot 10^{pK_a - pH}$ (see Ref. 79), the two quantities P_{RH+}, i.e. the decay rate constant of the protonated form and (pK_a – pH) are used as free-running parameters in the simulation procedure. The simultaneous fit of all W-band spectra to Eqn (7) ultimately results in p$K_a = 2.15 \pm 0.05$, which is in the perfect agreement with the X-band value (Fig. 8(c) and (d)). The lifetime of the protonated form, γ_e/P_{RH+}, was found to be 65 ± 10 ns, and to be independent of the pH value of the solution, as is expected from the protonation reaction scheme.

The solid-state EPR spectra at low temperatures (T = 120 K) differ strongly from the liquid case at room temperature; see Figs 8 and 9. In the rigid limit, the chemical exchange is very slow. Thus, the experimental nitroxide spectra have to be described by a weighted sum of RH^+ and R spectra. In X-band, where only the A_{zz} canonical positions can be spectrally resolved, the analysis does not yield unequivocal results because the changes in A_{zz} are small compared to the linewidth of the EPR signals and, moreover, are different for the low- and high-field EPR lines (Fig. 9(a)). Hence, a pK_a value of 3.5 ± 0.5 could only be estimated. However, the W-band spectra of shock-frozen samples show well recognizable shifts of both the g_{xx} and A_{zz} tensor components, due to the increased spectral resolution at high Zeeman field. Upon protonation, i.e. when comparing spectra at pH = 7.2 with those at pH = 1.3, it is seen that the g_{xx} peak shifts

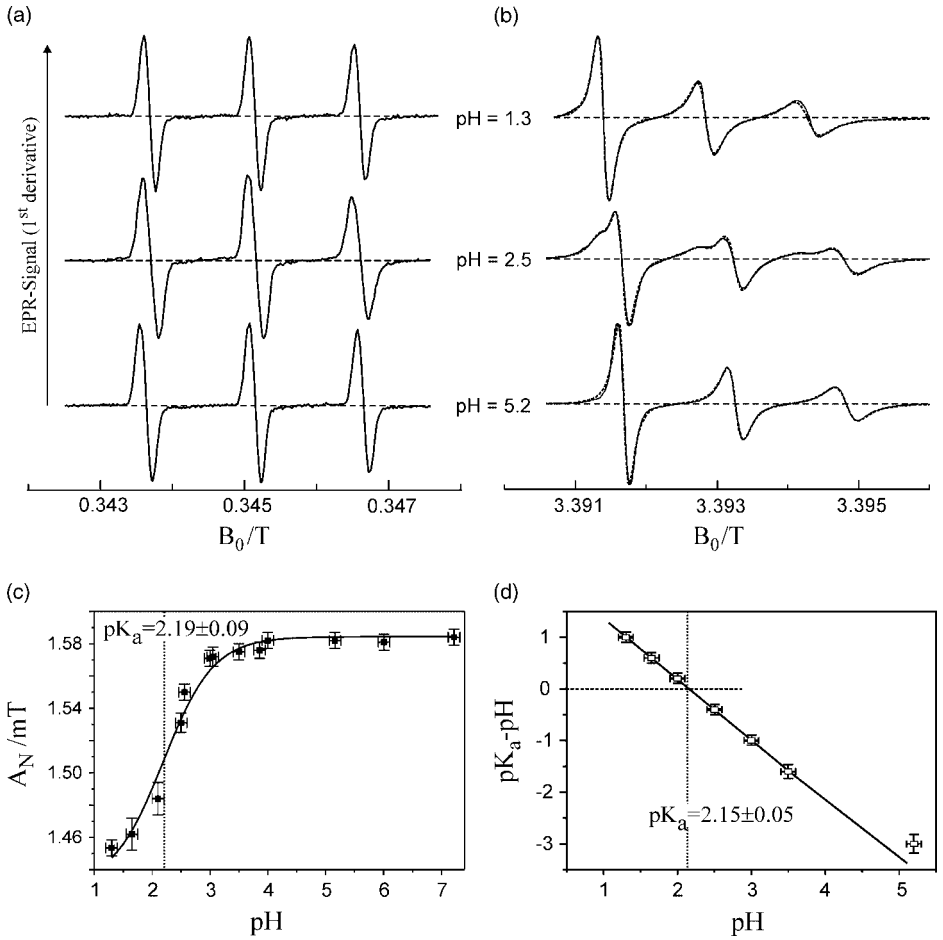

Figure 8. EPR studies of the pH-sensitive nitroxide spin-label IMTSL (see also Fig. 9(c)). X-band (a) and W-band (b) cw EPR spectra of 1 mM IMTSL water-buffer solution at room temperature corresponding to the fully protonated (pH = 1.3) nitroxide form, the unprotonated (pH = 5.2) nitroxide form, and the intermediate case (pH = 2.5). (c) pH-induced variation of the isotropic hyperfine constant A_N, measured as the distance between crossing point of the baseline of the central and high-field lines of the X-band EPR triplet, together with the corresponding Henderson–Hasselbalch titration curve. (d) Summarized results of 2-parameter fits of the W-band EPR spectra to modified Bloch equations containing a chemical exchange term; the simulated spectra are shown by dashed lines in (b) and are in perfect agreement with the experimental spectra. For details of the simulation procedure, see text.

approximately by −1.1 mT, and A_{zz} decreases by about 0.3 mT. The shifts in the g_{zz} and g_{yy} spectral regions cannot be observed within experimental resolution. The increase of the g_{xx} value by 6.4×10^{-4} upon protonation agrees fully with the shift of 6.5×10^{-4} reported by Gulla and Budil for a similar imidazolidine nitroxide.[81] The W-band EPR spectra obtained at intermediate pH values could be perfectly least-squares fitted to the weighted sum of the RH^+ and R spectra (Fig. 9(b)). The fraction of the unprotonated radical form is well described by a conventional titration curve with $pK_a = 3.48 \pm 0.05$. This value is higher than in liquid solution. The difference may be explained by the temperature-dependent exchange rate according to Eyring theory.

After having obtained such basic information about the protonation behavior of the IMTSL nitroxide in solution by our EPR experiments, we used this pH-sensitive label to investigate the local pH values within the proton channel of BR. The amino acid position D96 is of particular interest because, during the transition from the M to N state of the BR photocycle, reprotonation of the Schiff base occurs via proton transfer from the aspartic acid D96. During the BR initial-state recovery, D96 is reprotonated from the cytoplasmic side of the membrane. The spin-labeled BR was stabilized in acidic (pH = 3.0), neutral (pH = 6.8) and basic (pH = 10.0) water-buffer solutions. Figure 10(a) shows the room-temperature X-band EPR spectrum of IMTSL covalently attached to the BR D96C mutant at pH = 6.8. The spectrum is typical for an immobilized nitroxide spin label, in agreement with the location of the spin label deeply buried in the protein interior. However, small-amplitude reorientational oscillations of the nitroxide ring may still be present, which lead to partial averaging of anisotropic components of the **g** and **A** tensors. Therefore, only low-temperature (T = 120 K) X- and W-band spectra were analyzed to avoid complications in the lineshape analysis that are caused by the influence of nitroxide residual mobility and proton exchange processes on the EPR spectra. The low-temperature X-band spectra show minor changes upon changing the solvent pH. While the low-field line and the centerline of the spectrum stay unchanged over the studied pH range, the high-field line shifts toward the position of the protonated form when

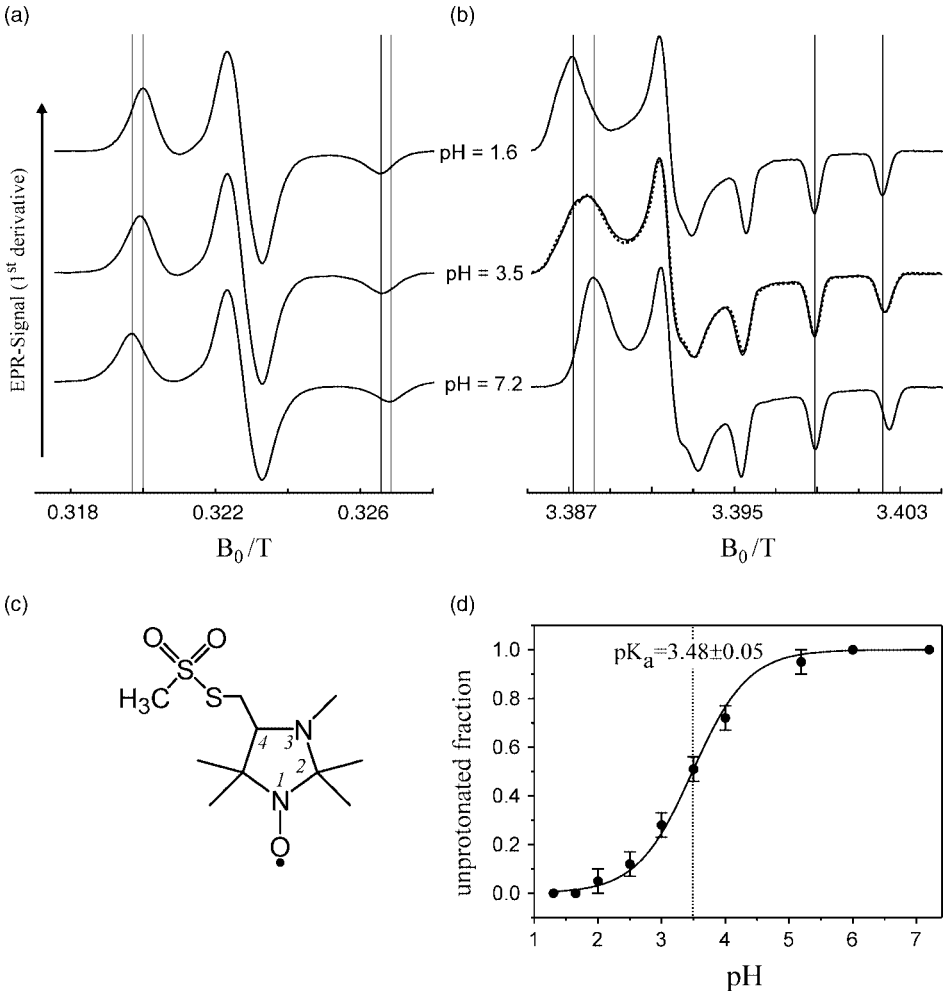

Figure 9. X-band (a) and W-band (b) cw EPR spectra of 0.3 mM IMTSL in water-buffer frozen solution, 120 K, corresponding to the fully protonated (pH = 1.65), the unprotonated (pH = 7.2) forms of the nitroxide ring and the intermediate case (pH = 3.5). The dashed lineshape for pH = 3.5 (b) is obtained by averaging the protonated and unprotonated spectra with equal weight. (c) Molecular structure of IMTSL. (d) The pH dependence of the fraction of the unprotonated IMTSL form as obtained from W-band EPR spectra analysis. The solid line is the fit to a conventional titration curve.

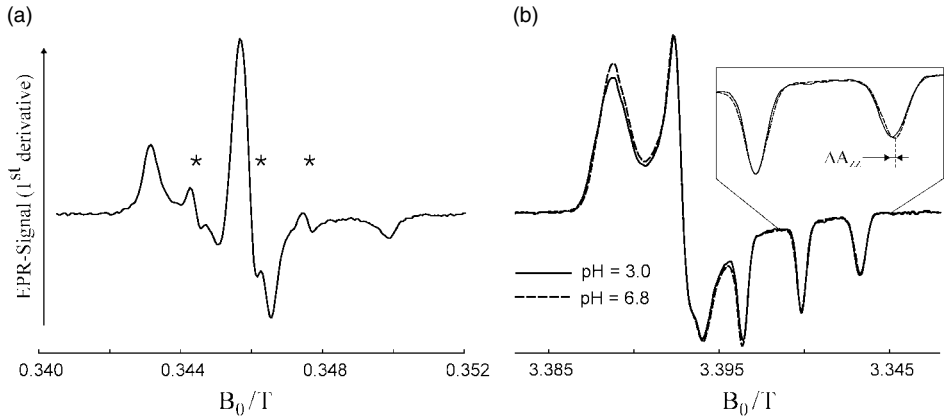

Figure 10. (a): X-band cw EPR spectrum of the IMTSL-labeled BR mutant D96C taken at room temperature and neutral pH. The stars mark the EPR line positions of unbound IMTSL in the sample solution. (b): W-band cw EPR spectra at acidic and neutral pH values of the buffer solution measured at 120 K (see text).

changing the solution pH from neutral to acidic. In agreement with X-band results, no difference in the W-band EPR spectra were observed at pH values higher than 6.8. Figure 10(b) shows the W-band spectra taken at acidic (pH = 3.0) and neutral (6.8) pH of the solution. A distinct shift of the A_{zz} lines can be observed. The value of A_{zz} slightly decreases from 3.42 ± 0.01 mT to 3.48 ± 0.01 mT upon lowering the pH. This decrease, together with changes in the g_{xx} spectral

region (Fig. 10(b)) shows that at acidic pH values the equilibrium between unprotonated and protonated states of the spin label is slightly shifted. Our attempts to simulate the spectra using the weighted sum of the spectra of protonated and unprotonated unbound IMTSL were unsuccessful, presumably owing to the effect of a different polarity of the microenvironment. However, from the values of A_{zz} and the lineshape of the g_{xx} region, one can conclude that the spin label is unprotonated throughout the physiological pH range of the solution. The small spectral changes after acidification of the solution prove the strong shielding of the nitroxide side chain at position 96 from the aqueous phase in the BR initial-state conformation.

This preliminary account of our ongoing multi-frequency EPR studies on pH-sensitive spin labels shall be summarized by the following statements:

1. To detect ionization-state changes of pH-sensitive spin labels attached to the protein, the EPR measurements have to be carried out at low temperature and high fields to provide sufficient spectral resolution. At room temperature, the attached spin label is often only partially immobilized, and the expected spectral changes due to changes of the ionization state are generally smaller than can be resolved within the linewidth in the slow-motion regime. High-field EPR is required to gain the spectral resolution necessary to separate the spectra of protonated and unprotonated states of the nitroxides. X-band EPR can hardly detect the difference in A_{zz} of maximal 0.3 mT, which is smaller than the linewidth of about 0.8 mT of the spectrally resolved $m_I = -1, +1$ lines of the nitroxide spectrum in the rigid limit. By W-band EPR, both g_{xx} and A_{zz} parameter changes can be quantitatively determined. Moreover, the g_{xx} tensor components of the protonated and unprotonated form can almost be resolved, since the corresponding field values differ by about 1.1 mT. This is comparable to the linewidth of about 1.6 mT of the g_{xx} resonance line.
2. For IMTSL, a further increase of the EPR frequency and Zeeman field beyond W-band EPR will probably not yield an advantage concerning the resolution of g_{xx} because of additional line broadening due to g-strain effects (Fig. 2). Such unwanted linearly field-dependent broadening will ultimately obscure the sensitivity of g_{xx} for probing local polarity, proticity and pH characteristics of the microenvironment of the spin-label. Hence, for high-frequency EPR, an optimum Zeeman field that represents a compromise between resolving power for g_{xx} to measure such environmental effects and onset of intolerable g-strain broadening of the g_{xx} component has to be chosen. For example, 220-GHz EPR spectroscopy on an imidazolidine nitroxide did not resolve the spectral g_{xx} region.[81] The use of isotope-substituted nitroxides, however, looks very promising for future applications of pH-sensitive spin labels. For example, deuteration of the nitroxide methyl positions decreases the width of the A_{zz} line to about 0.4 mT, which is comparable to the A_{zz} shift upon protonation (Fig. 1(a)). Moreover, deuteration of the methyl positions will allow the resolving of the g_{xx} lines of protonated and unprotonated forms of pH-sensitive spin labels by W-band EPR. Additional ^{15}N-substitution of the N-1 nitroxide position will lead to even higher resolution in the g_{xx} spectral region (Fig. 1(b)).
3. W-band EPR application of pH-sensitive spin labels opens a new avenue for the investigation of site-directed spin-labeled proteins. The pK_a values of imidazoline and imidazolidine radicals are strongly dependent on the substituents at C-4 of the radical heterocycle.[76] Such applications require systematic investigations of titration curves with the spin label attached to different water-accessible segments of the protein under study. Local polarity effects of the microenvironment may influence the pK_a of the nitroxide, in addition to the observed electric field dependent changes of the g_{xx} and A_{zz} values, making it a challenging task to use such labels to correlate pK_a changes with conformational changes of the protein in action.

CONCLUSIONS AND OUTLOOK

In this overview, it is shown that modern multi-frequency EPR spectroscopy at high magnetic fields provides detailed information about structure and dynamics of transient intermediates occurring in biological ion-transfer processes. Thereby our understanding of the relation between structure, dynamics and function of proteins undergoing conformational switching during biological action is considerably improved. This holds for the fine-tuning of electronic properties of cofactors involved in the transfer process by means of weak interactions with their protein and lipid environment, such as H-bonding to specific amino acid residues. This also holds with respect to the massive protein refolding in the course of transmembrane ion-channel formation. To summarize the conclusions relevant to biological systems in general and to the transfer proteins and channel-forming proteins referred in this paper in particular, the following observations are made:

- By high-field/high-frequency EPR even on disordered samples orientation-selective hydrogen bonding and polar interactions in the protein binding sites can be traced. This is important information complementary to what is available from high-resolution X-ray diffraction of protein single crystals.
- In electron-transfer processes, often several organic radical species are generated as transient intermediates. To distinguish them by the small differences in their g-factor and hyperfine interactions, high-field/high-frequency EPR becomes the method of choice.
- High-field/high-frequency cw EPR provides, by lineshape analysis, shorter time windows than X-band EPR do, down into the ps range for studying correlation times and fluctuating local fields over a wide temperature range. The correlation times are associated with characteristic dynamic processes, such as protein, cofactor or lipid motion and protein folding.
- Pulsed high-field/high-frequency EPR provides real-time access to specific cofactor and/or protein motions in the nanosecond timescale. Motional anisotropy, which is governed by anisotropic interactions, such as hydrogen

bonding along specific molecular axes within the binding site, can be resolved.
- ENDOR at high Zeeman fields takes additional advantage of the orientation selection of molecular subensembles in powder or frozen solution samples. Thereby, even in the case of small g-anisotropies, ENDOR on paramagnetic species can provide single-crystal like information about hyperfine interactions, including functionally important hydrogen bonding to the protein.
- High-field EPR adds substantially to the capability of 'classical' spectroscopic and diffraction techniques for determining structure–dynamics–function relations of biosystems, since transient intermediates can be observed in real time while they are staying in their *working states* at biologically relevant timescales.

As an outlook, some of our ongoing high-field EPR experiments that are related to the subject of this publication are mentioned.

At FU Berlin, ongoing high-field EPR spectroscopy refers to pulsed electron–electron double resonance (PELDOR) experiments at W-band on doubly spin-labeled proteins employing both pulsed double-frequency and field-jump methodologies.[82] PELDOR at X-band frequencies has proven to be very powerful for measuring weak electron spin–spin interactions between remote paramagnetic centers in disordered solids. Thereby, long distances up to 5-8 nm can be measured.[16,83] Exploiting the improved **g**-tensor resolution at high Zeeman fields, W-band PELDOR experiments give access to both distance and relative orientation of the protein fragments labeled with the two interacting nitroxide side chains.[82] Moreover, valuable information of distance and orientation of spin-labeled radical-pair systems is obtained from ongoing 360-GHz cw experiments at low temperatures. Thermal spin polarization effects are exploited to determine the sign of the zero-field splitting parameter D of two-spin systems[84,85] and, thereby, to discriminate between a disk-shaped dipolar tensor ($D > 0$, triplet state complex) and a cigar-shaped one ($D < 0$, radical-pair state complex). Thermal spin polarization effects on the EPR lineshape become strong at temperatures below the Zeeman temperature $T_Z = g \cdot \mu_B \cdot B_0/k_B$ (k_B Boltzmann constant). Thus, high-field EPR spectra show such polarization effects already at higher temperatures than X-band EPR spectra do (for $g \approx 2$ systems, $T_z \approx 0.4$ K for X-band, 4 K for W-band, and 16 K for 360 GHz EPR).

At Osnabrück, ongoing experiments comprise the characterization of the conformational dynamics involved in signal transfer by the sensory rhodopsin-transducer complex[86] and high-field EPR spectroscopy of spin-labeled proteins performing their function in their native cell environment.

Acknowledgements

We thank S. Weber (FU Berlin), T. F. Prisner (Frankfurt/M) for valuable experimental contributions over the years and D. Oesterhelt, J. Tittor and M. Pfeiffer (MPI Martinsried) for providing site-specific mutants of bacteriorhodopsin. We gratefully acknowledge the support of the Deutsche Forschungsgemeinschaft in the frame of the Schwerpunktprogramm SPP 1051 ('High-field EPR in Biology, Chemistry and Physics').

REFERENCES

1. Michel-Beyerle M-E (ed.). *The Reaction Center of Photosynthetic Bacteria, Structure and Dynamics*. Springer: Berlin, 1996.
2. Mäntele W. *The Photosynthetic Reaction Center*, vol. 2, Deisenhofer J, Norris JR (eds). Academic Press: New York, 1993; 239.
3. Rödig C, Chizhov I, Weidlich O, Siebert F. *Biophys. J.* 1999; **76**: 2687.
4. Remy A, Gerwert K. *Nat. Struct. Biol.* 2003; **10**: 637.
5. Lakey JH, Duché D, González-Manas J-M, Baty D, Pattus F. *J. Mol. Biol.* 1993; **230**: 1055.
6. Groot HJMd. *Curr. Opin. Struct. Biol.* 2000; **10**: 593.
7. Lansing JC, Hu JG, Belenky M, Griffin RG, Herzfeld J. *Biochemistry* 2003; **42**: 3586.
8. Mason AJ, Grage SL, Straus SK, Glaubitz C, Watts A. *Biophys. J.* 2004; **86**: 1610.
9. Möbius K. *Chem. Soc. Rev.* 2000; **29**: 129.
10. Riedi PC, Smith GM. *Electron Paramagnetic Resonance, A Specialist Periodical Report*. vol. 18, Atherton NM, Davies MJ, Gilbert BC, McLauchlan KA (eds). The Royal Society of Chemistry: London, 2002; 254.
11. Steinhoff H-J. *Front. Biosci.* 2002; **7**: 97.
12. Smirnov AI. *Electron Paramagnetic Resonance, A Specialist Periodical Report*, vol. 18, Gilbert BC, Davies MJ, McLauchlan KA (eds). The Royal Society of Chemistry: London, 2002; 109.
13. Pilbrow JR. *Transition Ion Electron Paramagnetic Resonance*. Clarendon Press: Oxford, 1990; 48.
14. Hubbell WL, Altenbach C. *Curr. Opin. Struct. Biol.* 1994; **4**: 556.
15. Freed JH. *Annu. Rev. Phys. Chem.* 2000; **51**: 655.
16. Borbat PP, Costa-Filho AJ, Earle KA, Moscicki JK, Freed JH. *Science* 2001; **291**: 266.
17. Cornish V, Bentson D, Altenbach C, Hideg K, Hubbell W, Schultz P. *Proc. Natl. Acad. Sci. U. S. A.* 1994; **91**: 2910.
18. Shafer AM, Kálai T, Liu SQB, Hideg K, Voss JC. *Biochemistry* 2004; **43**: 8470.
19. Hubbell WL, Cafiso DS, Altenbach C. *Nat. Struct. Biol.* 2000; **7**: 735.
20. Hubbell WL, Gross A, Langen R, Leitzow MA. *Curr. Opin. Struct. Biol.* 1998; **8**: 649.
21. Hubbell WL, McHaourab HS, Altenbach C, Leitzow MA. *Structure* 1996; **4**: 779.
22. Savitsky A, Kühn M, Duché D, Möbius K, Steinhoff HJ. *J. Phys. Chem. B* 2004; **108**: 9541.
23. Steinhoff H-J, Savitsky A, Wegener C, Pfeiffer M, Plato M, Möbius K. *Biochim. Biophys. Acta* 2000; **1457**: 253.
24. Wegener C, Savitsky A, Pfeiffer M, Möbius K, Steinhoff H-J. *Appl. Magn. Reson.* 2001; **21**: 441.
25. Plato M, Steinhoff H-J, Wegener C, Törring JT, Savitsky A, Möbius K. *Mol. Phys.* 2002; **100**: 3711.
26. Earle KA, Smirnov AI. *Very High Frequency (VHF) ESR/EPR, Biological Magnetic Resonance*, vol. 22, Grinberg O, Berliner LJ (eds). Kluwer/Plenum Publishers: New York, 2004; 96.
27. Livshits VA, Marsh D. *Very High Frequency (VHF) ESR/EPR, Biological Magnetic Resonance*, vol. 22, Grinberg O, Berliner LJ (eds). Kluwer/Plenum Publishers: New York, 2004; 431.
28. Barnes J, Liang Z, Mchaourab H, Freed J, Hubbell W. *Biophys. J.* 1999; **76**: 3298.
29. Stehlik D, Möbius K. *Annu. Rev. Phys. Chem.* 1997; **48**: 745.
30. Lebedev YS. *Foundations of Modern EPR*, Eaton SS, Salikhov KM (eds). World Scientific: Singapore, 1998; 731.
31. Smith GM, Riedi PC. *Electron Paramagnetic Resonance, A Specialist Periodical Report*, vol. 17, Atherton NM, Davies MJ, Gilbert BC, McLauchlan KA (eds). The Royal Society of Chemistry: London, 2000; 164.
32. Prisner T, Rohrer M, MacMillan F. *Annu. Rev. Phys. Chem.* 2001; **52**: 279.
33. Freed JH. *Very High Frequency (VHF) ESR/EPR, Biological Magnetic Resonance*, vol. 22, Grinberg O, Berliner LJ (eds). Kluwer/Plenum Publishers: New York, 2004; 19.
34. Möbius K, Savitsky A, Fuchs M. *Very High Frequency (VHF) ESR/EPR, Biological Magnetic Resonance*, vol. 22, Grinberg O,

Berliner LJ (eds). Kluwer/Plenum Publishers: New York, 2004; 45.
35. Gullá AF, Budil DE. *Concept. Magn. Res. Part B: Magn. Res. Eng.* 2004; **22B**: 15.
36. Prisner TF. *Very High Frequency (VHF) ESR/EPR, Biological Magnetic Resonance*, vol. 22, Grinberg O, Berliner LJ (eds). Kluwer/Plenum Publishers: New York, 2004; 249.
37. Marsh D, Kurad D, Livshits VA. *Chem. Phys. Lipids* 2002; **116**: 93.
38. Bennati M, Prisner T. *Rep. Prog. Phys.* 2005; **68**: 411.
39. Möbius K, Savitsky A, Schnegg A, Plato M, Fuhs M. *Phys. Chem. Chem. Phys.* 2005; **7**: 19.
40. Pfeiffer M, Rink T, Gerwert K, Oesterhelt D, Steinhoff H-J. *J. Mol. Biol.* 1999; **287**: 163.
41. Berliner LJ, Gruenwald J, Hankovszky HO, Hideg K. *Anal. Biochem.* 1982; **119**: 450.
42. Hideg K, Hankovszky HO. *Spin Labeling, Biological Magnetic Resonance*, vol. 8, Berliner LJ, Reuben J (eds). Plenum Press: New York, 1989; 427.
43. Smirnov AI, Ruuge A, Reznikov VA, Voinov MA, Grigoriev IA. *J. Am. Chem. Soc.* 2004; **126**: 8872.
44. Luecke H, Schobert B, Richter H-T, Cartailler J-P, Lanyi JK. *J. Mol. Biol.* 1999; **291**: 899.
45. Váró G, Lanyi JK. *Biochemistry* 1991; **30**: 5008.
46. Druckmann S, Friedmann N, Lanyi JK, Needleman R, Ottolenghi M, Shewes M. *Photochem. Photobiol.* 1992; **56**: 1041.
47. Hessling B, Herbst J, Rammelsberg R, Gerwert K. *Biophys. J.* 1997; **73**: 2071.
48. Haupts U, Tittor J, Oesterhelt D. *Annu. Rev. Biophys. Biomol. Struct.* 1999; **28**: 367.
49. Subramaniam S, Henderson R. *Nature* 2000; **406**: 653.
50. Stone AJ. *Proc. R. Soc. London* 1963; **A 271**: 424.
51. Törring JT. PhD thesis. 'Untersuchungen zum g-Tensor des primänen Donors in bakteriellen Reaktionszentren.' Free University Berlin, Berlin, 1995.
52. Törring JT, Un S, Knüpling M, Plato M, Möbius K. *J. Chem. Phys.* 1997; **107**: 3905.
53. Griffith OH, Dehlinger PJ, Van SP. *J. Membr. Biol.* 1974; **15**: 159.
54. Un S, Atta M, Fontecave M, Rutherford AW. *J. Am. Chem. Soc.* 1995; **117**: 10 713.
55. Kawamura T, Matsunami S, Yonezawa T. *Bull. Chem. Soc. Jpn.* 1967; **40**: 1111.
56. Earle KA, Moscicki JK, Ge M, Budil DE, Freed JH. *Biophys. J.* 1994; **66**: 1213.
57. Ondar MA, Grinberg OY, Lebedev YS. *Sov. J. Chem. Phys.* 1985; **3**: 781.
58. Subramaniam S, Lindahl I, Bullough P, Faruqi AR, Tittor J, Oesterhelt D, Brown L, Lanyi J, Henderson R. *J. Mol. Biol.* 1999; **287**: 145.
59. Tittor J, Paula S, Subramaniam S, Heberle J, Henderson R, Oesterhelt D. *J. Mol. Biol.* 2002; **319**: 555.
60. Radzwill N, Gerwert K, Steinhoff H-J. *Biophys. J.* 2001; **80**: 2856.
61. Lakey JH, Groot GFvd, Pattus F. *Toxicology* 1994; **87**: 85.
62. Stroud RM. *Curr. Opin. Struct. Biol.* 1995; **5**: 514.
63. Stroud RM, Reiling K, Wiener M, Freymann D. *Curr. Opin. Struct. Biol.* 1998; **8**: 525.
64. Oh KJ, Zhan H, Cui C, Hideg K, Collier RJ, Hubbell WL. *Science* 1996; **273**: 810.
65. Huynh PD, Cui C, Zhan H, Oh KJ, Collier RJ, Finkelstein A. *J. Gen. Physiol.* 1997; **110**: 229.
66. Lacy DB, Stevens RC. *Curr. Opin. Struct. Biol.* 1998; **8**: 778.
67. Salwinski L, Hubbell WL. *Protein Sci.* 1999; **8**: 562.
68. Cramer WA, Heymann JB, Schendel SL, Deriy BN, Cohen FS, Elkins PA, Stauffacher CV. *Annu. Rev. Biophys. Biomol. Struct.* 1995; **24**: 611.
69. Wiener M, Freymann D, Ghosht P, Stroud RM. *Nature* 1997; **385**: 461.
70. Dankert JR, Uratani Y, Grabau C, Cramer WA, Hermodson M. *J. Biol. Chem.* 1982; **257**: 3857.
71. Nardi A, Slatin SL, Baty D, Duché D. *J. Mol. Biol.* 2001; **307**: 1293.
72. Parker MW, Postma JPM, Pattus F, Tucker AD, Tsernoglou D. *J. Mol. Biol.* 1992; **224**: 639.
73. Duché D, Parker MW, González-Manas J-M, Pattus F, Baty D. *J. Biol. Chem.* 1994; **269**: 6332.
74. Todd AP, Cong J, Levinthal F, Levinthal C, Hubbell WL. *Proteins* 1989; **6**: 294.
75. Shin YK, Levinthal C, Levinthal F, Hubbell WL. *Science* 1993; **259**: 960.
76. Khramtsov VV, Volodarsky LB. *Spin Labeling: The Next Millenium, Biological Magnetic Resonance*, vol. 14, Berliner LJ (ed.). Plenum Press: New York, 1998; 109.
77. Khramtsov VV, Weiner LM, Grigoriev IA, Volodarsky LB. *Chem. Phys. Lett.* 1982; **91**: 69.
78. Savitsky A, Wegener C, Dubinskii AA, Grigoriev IA, Steinhoff H-J, Möbius K. *J. Phys. Chem.* 2005; to be published.
79. Atkins PW. *Physical Chemistry*. Oxford University Press: Oxford, 1986; 274.
80. Carrington A, McLachlan AD. *Introduction to Magnetic Resonance*. Harper and Row: New York, 1969; 204.
81. Gullá AF, Budil DE. *J. Phys. Chem. B* 2001; **105**: 8056.
82. Dubinskii AA, Grishin YA, Savitsky AN, Möbius K. *Appl. Magn. Reson.* 2002; **22**: 369.
83. Schweiger A, Jeschke G. *Principles of Pulse Electron Paramagnetic Resonance*. Oxford University Press: Oxford, 2001.
84. Hornig AW, Hyde JS. *Mol. Phys.* 1963; **6**: 33.
85. Chemerisov SD, Grinberg OY, Tipikin DS, Lebedev YS, Kurreck H, Möbius K. *Chem. Phys. Lett.* 1994; **218**: 353.
86. Klare J, Gordeliy VI, Labahn J, Büldt G, Steinhoff H-J, Engelhard M. *FEBS Lett.* 2004; **564**: 219.